MATERIALS SCIENCE

Metal-organic frameworks tailor the properties of aluminum nanocrystals

Hossein Robatjazi[1,2], Daniel Weinberg[2,3], Dayne F. Swearer[2,3], Christian Jacobson[2,3], Ming Zhang[2,4], Shu Tian[2,3], Linan Zhou[2,3], Peter Nordlander[1,2,4,5], Naomi J. Halas[1,2,3,4,5]*

Metal-organic frameworks (MOFs) and metal nanoparticles are two classes of materials that have received considerable recent attention, each for controlling chemical reactivities, albeit in very different ways. Here, we report the growth of MOF shell layers surrounding aluminum nanocrystals (Al NCs), an Earth-abundant metal with energetic, plasmonic, and photocatalytic properties. The MOF shell growth proceeds by means of dissolution-and-growth chemistry that uses the intrinsic surface oxide of the NC to obtain the Al^{3+} ions accommodated into the MOF nodes. Changes in the Al NC plasmon resonance provide an intrinsic optical probe of its dissolution and growth kinetics. This same chemistry enables a highly controlled oxidation of the Al NCs, providing a precise method for reducing NC size in a shape-preserving manner. The MOF shell encapsulation of the Al NCs results in increased efficiencies for plasmon-enhanced photocatalysis, which is observed for the hydrogen-deuterium exchange and reverse water-gas shift reactions.

INTRODUCTION

Metallic nanoparticles have been a major and ever-increasing research focus because of their enhanced reactivity relative to larger mesoscale and bulk phase materials (1). Over the past decade, much chemistry research has been concerned with the growth and reshaping of metallic nanoparticles and the inherent modifications of chemical reactivity that may result from changes in their size and shape (2). In addition, recent advances in photochemistry have relied on the collective electronic resonances (plasmons) of metallic nanoparticles to drive otherwise energetically unfavorable chemical reactions at temperatures and pressures far below those that typify conventional catalysis (3–5). In a parallel and equally dominant research focus, metal-organic frameworks (MOFs) have been synthesized and studied intensively for their ability to modify and enhance chemical reactivities (6). MOFs are complex three-dimensional (3D) networks with regular pores and channels that consist of crystalline lattices of metal cation centers ("nodes") connected by multitopic organic linkers. Since MOFs have a range of intriguing properties including, but not limited to, exceptionally high porosity and surface area, they have been the subject of extensive studies for applications such as gas storage, chemical separations, and heterogeneous catalysis (7). The integration of noble metal nanoparticles within MOFs has been reported with concomitant enhancements of chemical and photocatalytic activities relative to either nanostructured material alone (8, 9).

There have recently been increased efforts to identify Earth-abundant materials that may be possible substitutes for more precious metals in applications such as plasmonics and photocatalysis. The efforts toward the controlled growth of Earth-abundant plasmonic nanomaterials, such as aluminum (10–12), copper (13), titanium nitride (14), and other materials, have begun to shift focus to their photocatalytic properties. Beyond the noble and coinage metals, however, the oxidation of metallic nanoparticles is a common occurrence, and the presence of surface or bulk oxides markedly alters their inherent properties, chemical reactivities, and photocatalytic activities toward certain chemical reactions. In this regard, aluminum, the most abundant metal in Earth's crust, is particularly intriguing. Historically, aluminum nanopowders in combination with oxidants have been studied extensively as a potent nanoenergetic material (15). However, more recent efforts have focused on their plasmonic properties, which can be obtained through precise synthesis methods and growth under highly pristine conditions (16). Because of the formation of a 2- to 4-nm passivating surface oxide that arrests further oxidation, aluminum nanocrystals (Al NCs) and nanostructures can be quite stable and useful for applications ranging from chemical sensing (17, 18) to optoelectronic devices (19) to vibrant full-color displays (20, 21) and even water desalination (22). Their role as plasmonically driven photocatalysts has been recently demonstrated, as photocatalysts themselves (23) and as plasmonic "antennas" when combined with catalytic nanoparticles and oxides in antenna-reactor complexes (24, 25).

Here, we investigate the bottom-up encapsulation of chemically synthesized Al NCs within a MOF layer. A MOF synthesis approach has been developed, where Al^{3+} ions are etched from the surface oxide and are incorporated into the MOF framework as it is grown, enabling MOF encapsulating layers of varying thicknesses to be synthesized. With the removal of the Al^{3+} ions from the surface, the surface oxide layer retreats further into the Al NC, resulting in a systematic and controlled reduction of Al NC size without changes in the NC shape. We demonstrate the utility of Al NC@MIL-53(Al) nanoparticles for photocatalysis, showing that the restricted diffusion of reactant species away from the substrate due to the presence of the MOF layer increases the photocatalytic reactivity of Al NCs toward hydrogen exchange and reverse water-gas shift (rWGS) reactions.

RESULTS AND DISCUSSION
Synthesis of Al NC@MOF

An illustration of MOF layer growth around Al NC is shown in Fig. 1. This synthetic approach is inspired by naturally occurring pseudomorphic

[1]Department of Electrical and Computer Engineering, Rice University, Houston, TX, USA. [2]Laboratory for Nanophotonics, Rice University, Houston, TX, USA. [3]Department of Chemistry, Rice University, Houston, TX, USA. [4]Department of Physics and Astronomy, Rice University, Houston, TX, USA. [5]Department of Materials Science and NanoEngineering, Rice University, Houston, TX, USA.
*Corresponding author. Email: halas@rice.edu

mineral replacement reactions, where the chemical structure of a mineral is changed without altering the spatial structure (26, 27). In this case, however, the dissolution of the Al NC surface oxide layer serves as a source of Al^{3+} for the backbone of the MOF, facilitating its growth and eliminating the need to introduce an additional metal precursor. In the presence of the organic linker, the kinetics of Al oxide layer dissolution is coupled to MOF layer growth, resulting in the formation of a uniform Al-based MOF shell layer around the Al core. Along with dissolution of the native oxide layer and MOF layer growth, the Al NC surface beneath the original native oxide is controllably oxidized, resulting in an overall reduction of the Al NC particle diameter (also illustrated in Fig. 1). This synthetic approach represents an opportunity to expand the surface chemistry of Al NCs and also provides a method for the highly controlled partial oxidation of Al NCs.

Al NCs were first synthesized using a previously reported method (28). Transformation of the surface oxide layer into an Al-based MOF layer was accomplished through a one-pot hydrothermal strategy under a reaction temperature of 60°C in a mixed N,N′-dimethylformamide (DMF)/H_2O solvent system (see Materials and Methods for synthetic details). Because of its well-studied coordination in conventional MOF synthesis, 1,4-benzenedicarboxylic acid (H_2BDC) was chosen as the organic linker. Once the MOF is grown, the terephthalate (BDC) linker serves as a rigid spacer that connects the 1D parallel chains of AlO_6 octahedra and gives rise to the rhombic pores characteristic of this MOF, known as aluminum terephthalate [Al(OH)(bdc)]$_n$ MOF [also known as MIL-53(Al)] (29) (Fig. 2A and fig. S1). This MOF is of particular interest because of its excellent thermal and chemical stability. It exhibits dynamic shifts between its large rhombic pore and narrow trapezoidal pore configurations, termed breathing modes, depending on the presence and nature of guest molecules and environmental conditions (29).

Powder x-ray diffraction (PXRD) patterns of activated hybrid nanoparticles show multiple diffraction peaks in the range of 2θ = 5° to 35° and 2θ = 35° to 90°, corresponding to the crystalline lattice of the MIL-53(Al) and the Al NC core, respectively (Fig. 2B), as revealed by a comparison of experimental and simulated PXRD patterns of the MOF region. However, the full width at half maximum (FWHM) of the experimentally measured diffraction peaks in the MOF region is relatively broad. Considering the amorphous nature of the intrinsic surface oxide of aluminum, it is expected that the MOF shell layer that replicates the oxide layer structure exhibits small crystalline domains. Al crystallinity is well preserved during the MOF formation process: All indices corresponding to metallic face-centered cubic Al appear in the PXRD pattern of Al NC@MIL-53(Al) with relative intensities of the peaks remaining the same as for pristine Al NCs. This observation verifies that the dissolution-and-growth process preserves the crystalline structure of the parent NC during MOF formation. The characteristic vibrational bands of the MIL-53(Al) MOF formed around Al NCs were identified using Fourier transform infrared (FTIR) and Raman spectroscopy (fig. S2). Thermogravimetric (TGA) analysis showed that the MIL-53(Al) shell layer was thermally stable up to 450°C (fig. S3).

Transmission electron micrographs (TEMs) show the formation of a conformal MOF shell surrounding the individual Al cores with no free MOF or remaining bare particles (Fig. 2, C and D, and fig. S4). Scanning electron micrographs (SEMs) reveal a drastic change in surface features from the typically smooth surface of Al NC to highly structured surfaces after MIL-53(Al) shell layer growth (Fig. 2, E and F, and fig. S5). The high-angle annular dark-field scanning transmission electron micrograph (HAADF-STEM) of an individual Al NC@MIL-53(Al) nanoparticle (Fig. 2G) shows a strong contrast between the bright Al core and the darker shell. Analysis of the 3D reconstruction of particle morphology using electron tomography
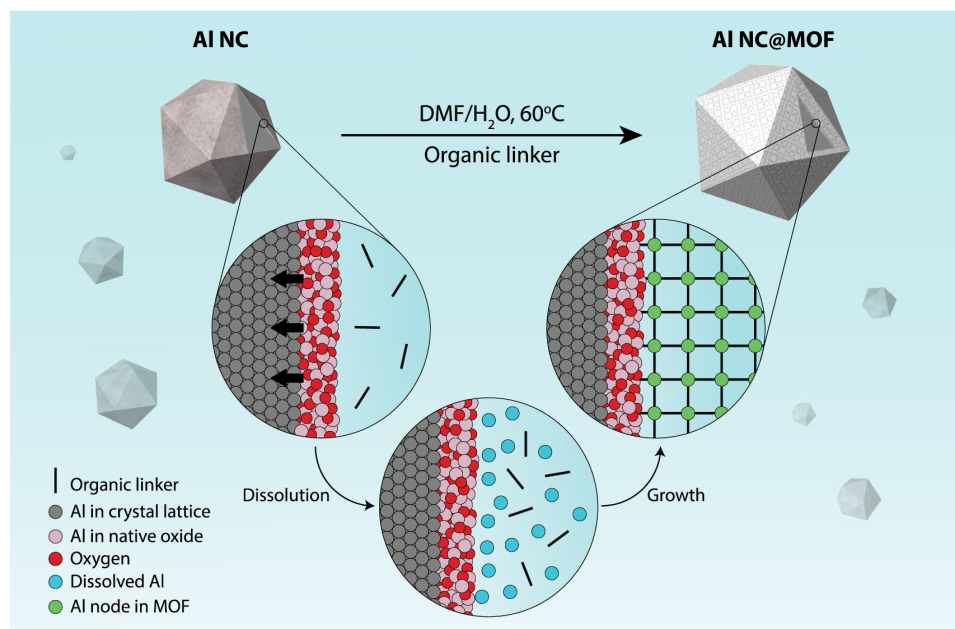

Fig. 1. Synthesis of Al NC@MOF plasmonic heterostructure based on dissolution-and-growth. The controlled dissolution of the oxide layer through a one-pot mild hydrothermal strategy in the presence of the requisite organic linker leads to the formation of a uniform Al-based MOF shell around the Al core. In this scenario, the native oxide layer serves as a source of Al^{3+} for the backbone of the MOF. As the dissolution of Al^{3+} progresses, the surface oxide is regrown onto the Al NC, controllably etching the nanoparticle, but always maintains a surface oxide protecting the metallic Al core.
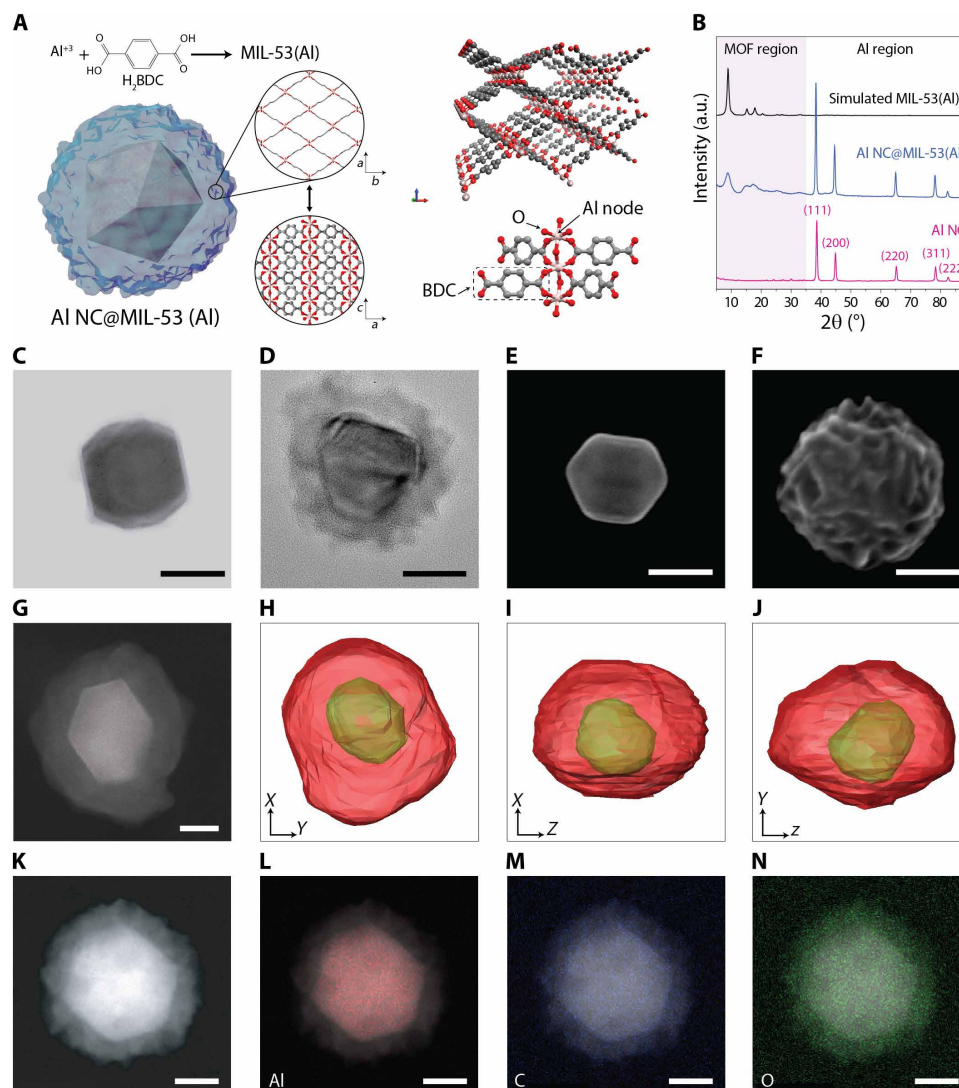
Fig. 2. Synthesis and characterization of Al NC@MIL-53(Al). (A) Schematic illustration of the structure of MIL-53(Al) grown around the Al core based on the dissolution-and-growth approach. Each aluminum center coordinates to two axial hydroxyl functionalities and four carboxylate units from linkers, sharing the coordination with the preceding and following Al centers in the chain. **(B)** Powder x-ray diffraction pattern of pristine Al NC, Al@MIL-53(Al) (activated for 4 hours at 150°C under vacuum), and simulated MIL-53(Al) in large-pore configuration. a.u., arbitrary units. **(C)** Transmission electron micrograph (TEM) image of single Al NC with the native oxide layer observable around the edge of the particle. **(D)** TEM image of single Al NC@MIL-53(Al). **(E)** Scanning electron micrograph (SEM) image of single Al NC. **(F)** SEM image of single Al NC@MIL-53(Al) showing a drastic change of the surface features compared with pristine Al NC. **(G to J)** High-angle annular dark-field scanning transmission electron micrograph (HAADF-STEM) image of (G) single Al NC@MIL-53(Al) and (H to J) surface rendering of Al NC@MIL-53(Al) in different orientations from electron tomography performed on the particle shown in (G). See movie S1. **(K to N)** HAADF-STEM image of a single Al NC@MIL-53(Al) particle (K) and energy-dispersive x-ray mapping of aluminum, carbon, and oxygen (L to N). Scale bars, 50 nm.

shows the position of the Al NC within its MOF matrix, where the MOF shell uniformly encapsulates the plasmonic core with no holes or gaps; however, the fine surface features observable by scanning electron microscopy (Fig. 2F) were not reproduced in the tomographic reconstruction (Fig. 2, H to J, and movie S1). Elemental mapping of the Al core and MOF shell also supports the structural characterization of a conformal MOF shell layer surrounding an Al NC core (Fig. 2, K to N).

In an alternate synthesis attempt, the previously established synthetic strategy for MIL-53(Al) was performed (*29*), where Al NCs were mixed with a metal nitrate precursor and the linker in an autoclave. Complete hydrothermal decomposition of the Al NCs was

observed because of their inherent instability in hot aqueous solution (fig. S6). The apparent inability to synthesize Al NC@MIL-53(Al) by conventional MOF synthetic routes reinforces the importance of the dissolution-and-growth strategy pursued here.

The dissolution-and-growth mechanism uses the 2- to 4-nm surface oxide layer that surrounds the Al NC core, which is independent of Al NC size. Therefore, under identical growth conditions, the MOF layer thicknesses should be uniform and independent of Al NC size as well. Figure 3 shows MIL-53(Al) shell layers grown around Al NCs varying in diameter from 50 to 150 nm, exhibiting dipolar plasmon resonances ranging from 350 to 680 nm in wavelength. The optical absorption of MIL-53(Al) is shown for comparison

(Fig. 3A). Despite the consistent reduction in diameter of the Al NCs following MOF growth, an overall red shift of the localized surface plasmon resonance (LSPR) is observed for all particle sizes after MOF growth, which is dominated by the increased refractive index of the dielectric environment because of the growth of the MOF shell layer.

Single-particle dark-field scattering measurements were also taken for bare Al NC and for similarly sized MOF-coated particles (Fig. 3E). For the bare Al NC, the scattering spectrum exhibits a pronounced dipolar mode around 3.3 eV and agrees very well with the calculated spectrum where the geometry of the particle is assumed to be spherical. The Al quadrupolar resonance around 5 eV lies outside the spectral window and cannot be seen. The MOF coating introduces substantial spectral changes. The quadrupolar and dipolar modes red-shift by around 1 eV and are now both visible in the spectrum. A pronounced narrowing of the dipolar plasmon linewidth is apparent. The calculated spectrum (modeling the MOF as a spherical shell of a refractive index of $n = 1.5$) shows the same spectral changes as the experiment. The slight disagreement for the intensity and energy of the quadrupolar resonance is most likely due to the particle having a nonspherical shape. Analysis of the spectra for a number of particles (Fig. 3, F and G) showed distinct improvements in the FWHM and corresponding quality factor (peak energy divided by

FWHM) for the MOF-coated particles compared to bare Al. Theoretical analysis showed that this effect is primarily due to the reduced radiative damping due to the LSPR red shift but with the slight size reduction of the Al core also contributing (30).

Kinetic control and MOF growth mechanism

The coupling between the kinetics of dissolution and growth can be modified by changing the pH of the initial reaction mixture. In nature, the dissolution of oxide minerals (known as chemical weathering) has been well studied in hydrogeochemical processes, where dissolution is influenced by pH and by concentration of dissolved ligands (31). In Al NC@MIL-53(Al) synthesis, adding increasing concentrations of acetic acid to the reaction mixture lowers the initial pH from ~4.1 to ~3.5 (in the presence of 30 mM acetic acid). This pH manipulation causes an increase in the rate of dissolution and also reduces the rate of MOF nucleation because of suppression of linker deprotonation. As the reaction proceeds, the pH of the solution gradually increases (fig. S7), increasing the concentration of the deprotonated linker, which can initiate MOF growth and inhibit further dissolution of the Al NC core. By exploiting the sensitivity of the plasmon resonance of the Al NC@MIL-53(Al) nanoparticle to its core size and its surrounding dielectric medium, we can monitor the pH-controlled kinetic balance of Al NC@MIL-53(Al) synthesis in detail (Fig. 4).
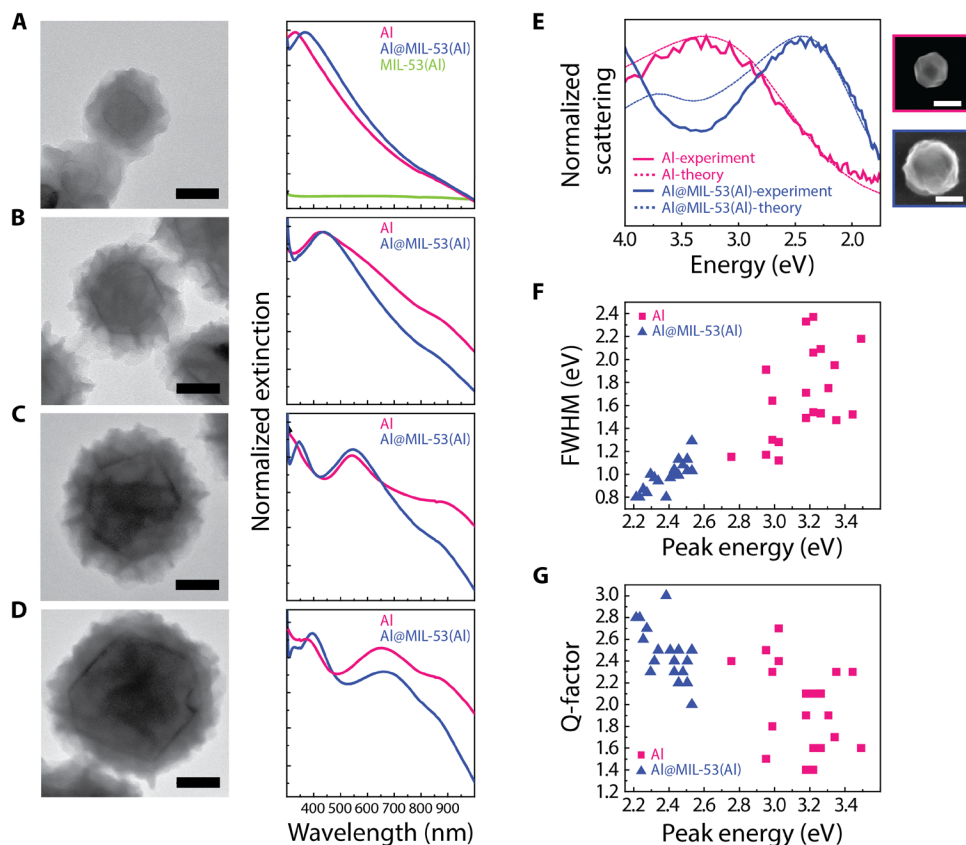

Fig. 3. Al NC@MIL-53(Al) with tunable surface plasmon resonance. (A to D) Representative TEM images of Al NC@MIL-53(Al) with nominal Al core sizes of (A) 50 nm, (B) 85 nm, (C)110 nm, and (D)150 nm and their corresponding normalized extinction spectra before and after MIL-53(Al) growth. The extinction spectrum of the pure MIL-53(Al) is provided in (A). Scale bars, 50 nm. For particles larger than 100 nm, additional peaks appearing at wavelengths <550 nm correspond to the quadrupolar plasmon resonance. Interband absorption of Al appears at nominally 820 nm. (**E**) Experimental and theoretical scattering spectrum of bare and MOF-coated particles, showing narrowing of the dipolar plasmon linewidth as a result of MOF growth around Al NC. SEM images of the nanoparticles used to obtain these spectra are shown on the right. Scale bar, 100 nm. (**F**) FWHM and (**G**) quality factor (peak energy divided by FWHM) for the MOF-coated Al NCs compared to pristine Al NCs.
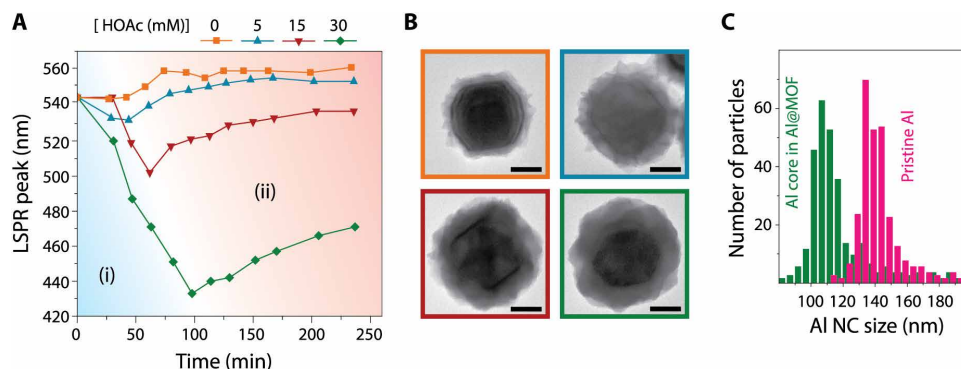
Fig. 4. Controlling the kinetics of Al NC dissolution during MOF formation. (A) Monitoring the LSPR shift of the Al core as a function of time during the formation of the MIL-53(Al) MOF shell in the presence of various concentrations of acetic acid (HOAc) in the initial reaction mixture. The magnitude of the LSPR shift is divided into regions (i) and (ii) representing the dissolution and growth steps, respectively (see fig. S8 for the complete extinction spectra). **(B)** Representative TEM images of Al NC@ MOF heterostructure formed in the absence of acetic acid (orange) and the presence of 5 mM (blue), 15 mM (red), and 30 mM (green) acetic acid. Addition of increasing quantities of acetic acid to the initial reaction mixture controllably increases the rate of dissolution of the oxide layer, causing a greater degree of Al core shrinkage and formation of a thicker and denser MOF shell. **(C)** Size distributions of pristine Al NC and Al core encapsulated in MOF grown in the presence of 30 mM acetic acid.

The LSPR shifts that occur during synthesis, for varying concentrations of acetic acid, are monitored (Fig. 4A). The LSPR blue shift in region (i) suggests that the reaction is dominated by the kinetics of Al dissolution, whereas the LSPR red shift in region (ii) indicates that little or no further Al dissolution is occurring, but rather, indicates MOF nucleation and growth. The growth dynamics of the Al-based MOF was previously studied using surface-enhanced Raman spectroscopy (32) to probe the vibrational modes of the free organic linker and metalated linker within the MOF enclosure. In contrast, monitoring the LSPR shift of the Al core provides an in situ probe for a simultaneous kinetic study of both Al^{3+} formation (from oxide layer dissolution) and subsequent metalation of the linker and enables differentiation of the dissolution-and-growth process into its component steps.

The magnitude of the initial LSPR blue shift increases with increasing acid concentration, indicating a greater degree of Al NC dissolution and a greater thickness of the MOF shell layer (Fig. 4B). The particle size distribution shows an ~30-nm average reduction of Al core diameter for MOFs grown in the presence of 30 mM acetic acid (Fig. 4C). This series of dissolution and growth studies indicates that this approach can serve as a method for controlled etching of Al NCs, providing a route for precise tuning of the plasmon energy of Al NCs to shorter wavelengths. In a control experiment in the absence of linker molecules, uncontrolled dissolution of Al NCs within the reaction time scale was observed (fig. S9). In contrast to acetic acid, the addition of sodium acetate to the reaction mixture inhibited MOF growth despite the higher concentration of free linker anion (fig. S10).

To further elucidate the specific mechanism for MOF formation around Al NCs, we investigated the progress of Al NC@MIL-53(Al) growth by quenching aliquots of the reactant mixture over the course of the reaction. We have identified a four-step mechanism based on pseudomorphic replacement, where corresponding electron micrographs of the nanoparticles obtained throughout the reaction revealed changes to the surface morphology at each step (Fig. 5). Oxide dissolution is initiated by fast hydration of the surface oxide (Al_2O_3 + H_2O ➔ $2AlOOH$), followed by a reaction between the newly generated aluminum oxyhydroxy [AlO(OH)] surface species and adsorbed H^+ to release Al^{3+} at the interface in the form of a metal aqua complex

(33). The fast coordination between the aluminum aqua complex ($[Al(H_2O)_6]^{3+}$) and the linker anion enriches the interface with the metal complex–linker species at a supersaturated concentration that promotes MOF crystal nucleation, followed by further growth. The drawing in Fig. 5D assumes a plausible MOF growth mechanism in a perpendicular manner, where 1D chains of the AlO(OH) extend perpendicular to the NC surface and are connected to each other via linker molecules (27, 32).

The dependence of the AlO(OH) dissolution on the adsorbed H^+ is consistent with the effect of the initial pH of the reaction mixture on MOF formation kinetics (Fig. 4 and figs. S7 and S10) and indicates the characteristic of high-degree pseudomorphic replacement, in which the primary dissolution process needs to be a rate-limiting step compared to the secondary growth step (26). We suggest that, independent of its dissolution rate, the oxide layer is continuously reestablished because of the thermodynamic equilibrium between oxide thickness and metal-ion diffusion from the surface layer of the metal into an interstitial position of the oxide (34). As a result, the regenerated surface oxide remains sufficiently thin (2 to 4 nm) for the continuous hydration-dissolution of noticeable oxide quantities (up to 30-nm reduction of Al core size in Fig. 4), which otherwise may not be accessible for a thicker oxide layer (32).

Gas uptake and plasmonic photocatalysis

Plasmonic metal nanoparticles have attracted significant attention for photocatalysis because of their capability to activate chemical transformations on their surfaces under illumination (35, 36). The plasmon resonant interaction of light with metallic nanoparticles leads to the generation of energetic hot carriers upon plasmon decay, which, along with photothermal heating, can drive otherwise energetically unfavorable chemical reactions. Recently, Al NCs have been demonstrated as an Earth-abundant, low-cost alternative to Ag and Au for plasmon-mediated photocatalysis (23). We have investigated Al NC@MIL-53(Al) nanoparticles for their gas uptake properties and to examine the effect of the MOF layer on their photocatalytic reactivity relative to pristine Al NCs (Fig. 6). The porosity of the MOF shell layers of the Al NC@MIL-53(Al) nanoparticles was confirmed and quantified by N_2 sorption (Fig. 6A) and CO_2 sorption (Fig. 6B) measurements (see fig. S11 for pore size distribution).
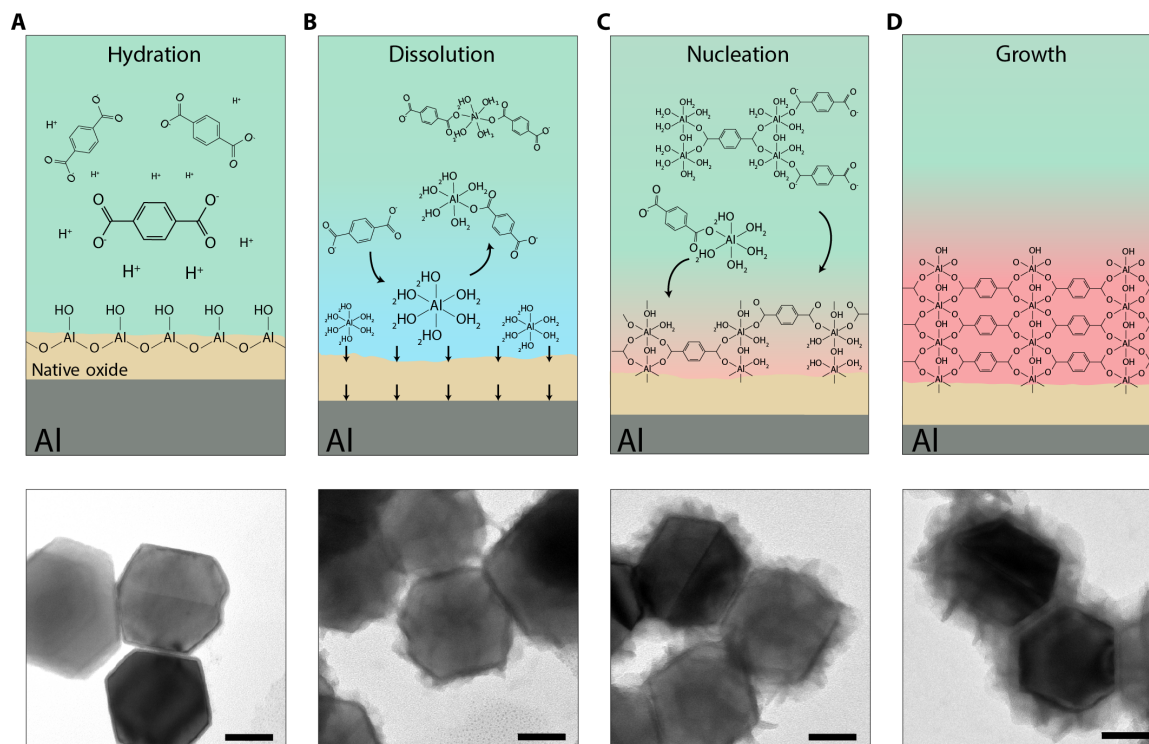
Fig. 5. Proposed mechanism of MOF [MIL-53(Al)] formation around Al NCs. (A to D) Schematic depicting the proposed dissolution-and-growth mechanism and corresponding TEM images (below) of nanoparticles obtained at various stages [(A) 20 min, (B) 40 min, (C) 60 min, and (D) 80 min] showing progressive MOF formation. The particle surface remains visibly unchanged during hydration of the surface oxide layer to aluminum oxyhydroxy [$Al_2O_3 + H_2O \rightarrow 2AlO(OH)$]. The dissolution of AlO(OH) by reacting with adsorbed H^+ generates an interface with a high concentration of the aluminum aqua complex ([$Al(H_2O)_6$]$^{3+}$) that then quickly coordinates with the linker molecule to form mono- or oligomers of the metal complex–linker species. Localized supersaturation of the solid/liquid interface with coordinated species promotes nucleation of the MOF crystal near the same dissolution site. The onset of the nucleation process after approximately 60 min of the reaction time is consistent with the onset of the LSPR red shift observed during MOF formation (orange dotted line in Fig. 4A). The nucleation process is followed by MOF layer growth that is nearly complete at 80 min into the reaction. We note that, because of thermodynamic equilibrium, the newly generated oxide layer is continuously reestablished while constantly dissolving to supply Al^{3+} for MOF growth. Scale bars, 50 nm.

The Al NC@MIL-53(Al) nanoparticle uptake follows a type II isotherm for N_2 sorption at 77 K, an indication of its microporous (rather than macroporous) nature (37). In contrast, the N_2 sorption isotherm on bare Al NCs follows type III behavior, characteristic of a nonporous surface (37). The gravimetric Brunauer-Emmett-Teller (BET) surface area increased from ~45 m^2 g^{-1} for pristine Al NCs to ~371 m^2 g^{-1} after MOF formation. The MIL-53 series of MOFs has been considered to be promising materials for CO_2 capture and storage (38). The low-pressure CO_2 sorption isotherm shows significant enhancement of CO_2 uptake capacity as a result of MOF growth (Fig. 6B). This enhancement originates from dipolar or quadrupolar interactions between CO_2 molecules and the hydroxyl groups (–OH) in the MIL-53(Al) framework (39).

The photocatalytic reactivity of the Al NC@MIL-53(Al) nanoparticles was characterized for two benchmark reactions of hydrogen dissociation and reduction of carbon dioxide in the rWGS reaction, where the Al NC@MIL-53(Al) nanoparticles outperform pristine Al NCs under visible light illumination (see fig. S12 for extinction spectrum of the photocatalysts and emission spectrum of the light source spectrum). The rate of hydrogen dissociation on Al NC@MIL-53(Al) nanoparticles as a function of visible light power under ambient conditions is significantly higher than that of pristine Al NCs without the MOF shell (Fig. 6C), particularly at higher illumination powers [the isotopic hydrogen exchange reaction $H_2 + D_2 \rightarrow 2HD$

was used to monitor hydrogen dissociation (23)]. Enhancement of the photocatalytic activity was also observed for the rWGS reaction relative to pristine Al NC (Fig. 6D), consistent with our CO_2 adsorption results. Similar to our previous work on plasmon-induced hot carrier–driven rWGS, we observed an increased selectivity in product formation under illumination over the traditional thermally driven reaction (25). Photocatalytic rWGS yields selective CO formation in contrast to the formation of both CH_4 and CO in thermally driven processes (fig. S13). Using pure MIL-53 (without Al NCs) as a control substrate, although significantly higher MOF weight loading can be achieved compared to Al NC@MIL-53(Al) nanoparticles, no rWGS photocatalytic activity is observed. This observation confirms the role of the Al NC core as the active plasmonic component in photocatalysis, where the MOF shell provides an enriched adsorbate concentration near the surface of the Al NC core.

Generalizability of Al NC@MOF
Through the choice of suitable organic linkers and reaction conditions, the present strategy demonstrates a degree of flexibility for MOF-coated Al NCs, including [$Al(OH)(1,4\text{-}NDC)$]$_n$ and ($Al_{12}O(OH)_{18}(H_2O)_3(Al_2(OH)_4)$[btc]$_6$·24$H_2O$) [known as MIL-96(Al)] (figs. S14 and S15). For example, applying our dissolution-and-growth approach to Al NCs in a solution with 1,4-naphthalenedicarboxylic acid (1,4-NDC) linkers promotes the formation of a uniform
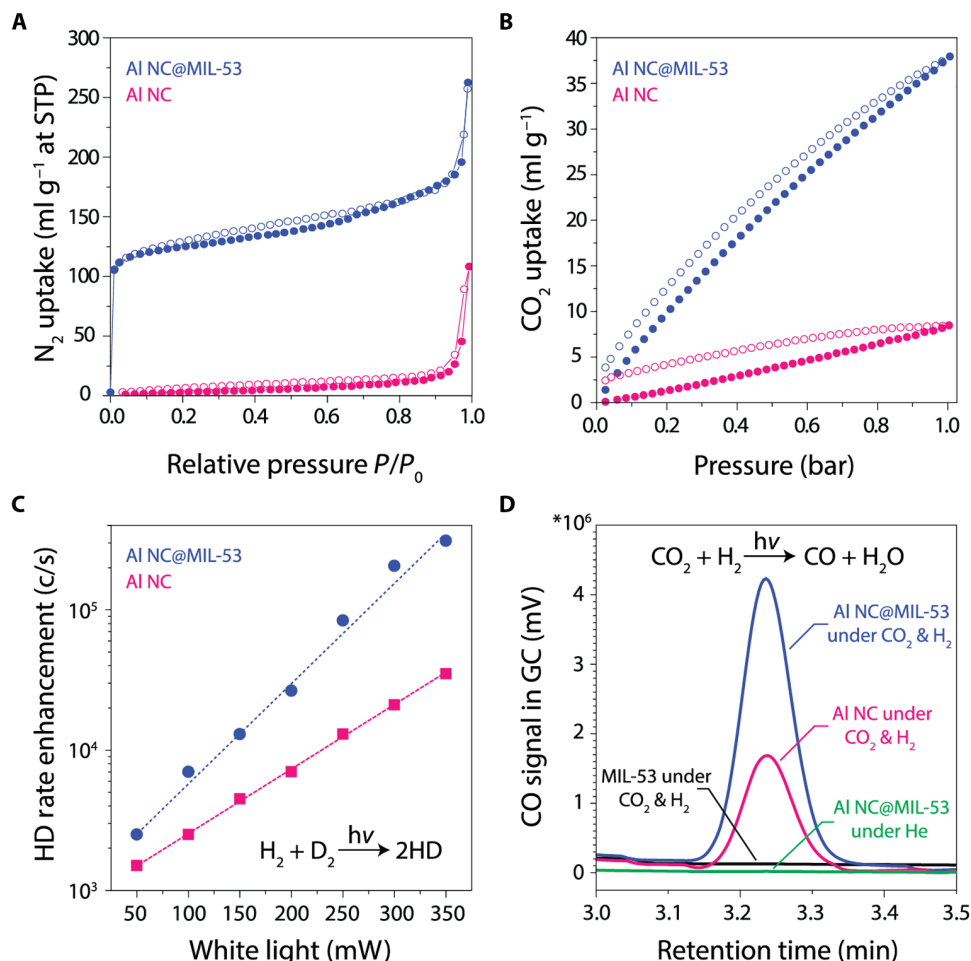
Fig. 6. Enhancing gas uptake and photocatalytic activity of Al NCs through MOF shell layer growth. (**A**) N_2 adsorption isotherm for Al NC@MIL-53(Al) and bare Al NCs measured at 77 K. STP, standard temperature and pressure. (**B**) Low-pressure CO_2 adsorption isotherm for Al NC@MIL-53(Al) and bare Al NC measured at 273 K. The solid and open symbols represent adsorption and desorption, respectively. (**C**) Photocatalytic reactivity of AlNC@MIL-53(Al) compared to pristine Al NC for the hydrogen-deuterium (HD) exchange reaction. (**D**) Photocatalytic reactivity of AlNC@MIL-53(Al) compared to pristine Al NC and pure MIL-53(Al) for the rWGS reaction under 300-mW white-light illumination. CO formation under illumination was detected when CO_2 and H_2 were both present. Illumination of the photocatalyst in an inert He atmosphere did not produce any measurable product, verifying that CO formation was not due to the decomposition of any organic contamination that may be present. GC, gas chromatography.

shell composed of a $[Al(OH)(1,4-NDC)]_n$ framework around the Al NC core. This MOF layer improves the stability of Al NCs in aqueous solution (fig. S16). MOF shell layers can also be grown in nanoparticle complexes such as antenna-reactor plasmonic photocatalysts, consisting, for example, of plasmonic nanoparticles or NCs bound with active transition metal (TM) nanoparticle islands (fig. S17) (*40*).

CONCLUSION
Here, we present a generalized approach based on dissolution and growth of the native oxide layer with a variety of different organic linkers. Given the pronounced effect of MOF composition and pore structure on properties and activity, we envision future variations in synthetic conditions and postsynthetic modifications that could result in a wide range of nanoparticles coated with MOF layers. This approach should generally be applicable to any metal nanoparticle with either a native or added oxide surface layer. Combining antenna-reactor photocatalyst complexes with MOF shell layers has enormous potential to significantly expand the types of plasmon-mediated

chemical reactions and improve their efficiencies and selectivities, an open and exciting area for future research.

MATERIALS AND METHODS
Al NC synthesis
Al NCs were synthesized according to our previously published protocol with minor modifications. (*28*) The size of particles was controlled by varying the ratio of tetrahydrofuran (THF)/1,4-dioxane solvents. All glassware, syringes, and needles were dried at 130°C overnight before use. THF and 1,4-dioxane solvents were sparged and dried over 4-Å molecular sieves and were kept in the glove box before use. In a typical experiment, 5 ml of anhydrous THF and 15 ml of anhydrous 1,4-dioxane (Sigma-Aldrich) were mixed in a dry Schlenk flask under argon atmosphere or in the glove box with standard techniques for handling air-sensitive materials. The solvent mixture was heated at 40°C, and 6.0 ml of 0.5 M dimethylethylamine alane in toluene (Sigma-Aldrich) was injected into the ethereal solvent. Next, 0.5 ml of 2 weight % (wt %) solution of Ti(IV) isopropoxide [Ti(OiPr)$_4$] in anhydrous toluene

(Sigma-Aldrich) was injected rapidly into the reaction mixture. The reaction was allowed to proceed for the next 2 hours during which the color of the solution turned from dark black to gray, indicating formation of Al NCs. The as-synthesized particles were transferred to a 50-ml centrifuge tube under a blanket of N_2, and nanoparticles were isolated by centrifugation at $500g$ for 5 min. The dark brown supernatant containing Ti catalysts and unreacted precursor was poured off, 40 ml of dry toluene was added, and the mixture was sonicated vigorously. The particles were isolated by centrifugation at $2000g$ for 10 min, followed by two cycles of washing and centrifuging in 2-propanol (IPA). Last, Al NCs were dispersed in IPA or DMF and stored at room temperature for future use. During post-synthetic work-up, the surface of the particles immediately oxidizes, and a 2- to 4-nm self-limiting amorphous Al_2O_3 layer forms.

Preparation of Al NC@MOF heterostructures

The general approach for the synthesis of Al@MOFs is based on a one-pot solvothermal strategy. For the synthesis of Al NC@[Al(OH)(bdc)]$_n$ in a typical synthesis, a suspension of Al NCs (0.1 mg/ml) was prepared in 12 ml of 1:1 (v/v) mixture of DMF and water. The mixture was transferred into a 20-ml vial containing 0.12 mmol of H_2BDC linker molecules. The mixture was then stirred or sonicated at 60°C for about 4 hours (sonication was preferred to assure homogeneity of the mixture and minimize particle aggregation because of the relatively high concentration of Al NCs in the reaction solution). The products were isolated via three cycles of washing and centrifuging in DMF. The final particles can be dispersed in DMF, IPA, dichloromethane, methanol, or ethanol. The synthesis can be readily scaled to liters if necessary. For large-scale synthesis, we recommend preparing the linker/DMF mixture first, followed by slow addition of the water in the ice bath to minimize the excess of heat generation from the exothermic water-DMF mixing process. Small variations in the concentration of NCs and linker molecules did not cause discernable effects on MOF growth. For additional shrinkage of the Al NC size by controlled etching of the subsurface metallic Al, various quantities of acetic acid (0.61, 1.83, and 3.66 mmol) were added to the initial reaction mixture containing 0.12 mmol of the linker. Synthesis of Al NC@[Al(OH)(1,4-NDC)]$_n$ and Al NC@MIL-96(Al) was performed under similar conditions to that of MIL-53(Al) by substituting the H_2BDC linker with 1,4-NDC and benzene-1,3,5-tricarboxylic acid (H_3BTC), respectively.

Preparation of MIL-53(Al) crystal powder

MIL-53(Al) MOF as a control for photocatalysis measurements was prepared according to the literature (29) with minor modifications. $Al_2(NO3)_3$ (1.3 g) and H_2BDC linker (0.288 g) were dissolved in 5 ml of water transferred to an autoclave. The reaction proceeded at 220°C for 48 hours. The MOF powder was collected and washed several times with DMF to remove the unreacted precursors and was vacuum-dried at 120°C for 2 hours. The final powder was stored under vacuum at room temperature before photocatalysis measurement.

Dark-field measurements

Dark-field scattering measurements were carried out on Electron Microscopy Sciences fused quartz substrates or Silicon Valley Microelectronics fused quartz substrates, prepared by sonication in acetone followed by an IPA wash and then by deposition of 50 nm of gold on top of a 3-nm Ti adhesion layer. The metal was deposited through a Ted Pella Micron Index 1 TEM grid to create a grid pattern, allowing

for particle identification. Dark-field samples were prepared by diluting reaction solutions between 50 and 500 times in IPA, sonicating 10 min in a bath sonicator (VWR Model 150D) and three 30-s bursts in a probe sonicator (Branson Sonifier 450) to prevent aggregation, and then drop-casting ~10 µl onto a prepared substrate. After drop casting, samples were dried under a light nitrogen stream.

Electromagnetic simulation

The scattering calculations were performed using a commercial finite-difference time-domain (FDTD) method software package (Lumerical FDTD Solutions 8.16.1022). The MOF-coated Al particles were modeled as concentric spheres placed on a SiO_2 substrate. The diameter of the Al core, the thickness of the Al_2O_3 layer, and the thickness of the MOF layer were chosen to be 120, 3, and 30 nm, respectively. A total-field scattered-field light source was used to simulate a plane wave with a 60° incident angle. The collected scattering was calculated by first calculating the far-field scattering of the particle in the air side and then integrating the scattering intensity between the minimum (15°) and maximum (40°) collection angles. To account for the unpolarized light used in the experiment, we obtained the final scattering spectrum by averaging the scattering spectrums calculated from four different polarization angles: 0° (p polarization), 90° (s polarization), 45°, and −45°. The dielectric responses of Al, Al_2O_3, and SiO_2 were taken from tabulated data (41, 16).

Catalyst preparation and reactor experiments

The as-synthesized Al NCs and Al NC@MOF particles were dried and activated under dynamic vacuum at 150°C for 4 hours before BET analysis. The photocatalysis experiments were performed on the same particles used for BET analysis. The catalysts were prepared by homogeneous dispersion of particles onto a γ-Al_2O_3 particle support (Alfa Aesar) at 50 wt % loading. The nanoparticles were mixed with the oxide support particles, and the mixture was ground thoroughly to homogenize the catalyst. Pure MIL-53(Al) MOF without oxide support was used as a control sample, and its activity was compared with the Al@MOF nanoparticles. All catalytic activities were measured at a total pressure of 1 atm using about 10 mg of the catalyst loaded into a customized stainless steel chamber flow fixed-bed reactor (Harrick Scientific Products Inc.). The reactor set-up synthesis was previously described (25). The photocatalytic experiments were performed at room temperature without external heating. The catalyst was illuminated using a supercontinuum fiber laser (400 to 850 nm, 4 ps, 40 MHz; Fianium) broadband visible light source with peak intensity at 700 nm (see fig. S11 for source spectrum), and a lens (150-mm focal length; Thorlabs) was used to focus the light to a 1.5-mm spot size onto the photocatalyst, through the quartz reactor window. Thermal activity measurements were conducted in the absence of light and by heating the chamber with a temperature controller (Harrick Scientific Products Inc.). For the hydrogen-deuterium exchange reaction and for the rWGS reaction, a 1:1 ratio of H_2/D_2 (research purity, Matheson Tri-Gas) and a 1:1 ratio of CO_2/H_2 (research purity, Matheson Tri-Gas), respectively, were continuously flowed into the reaction chamber at a total flow rate of 20 SCCM (standard cubic centimeters per minute). The effluent composition was measured in real time using a quadrupole mass spectrometer (Hiden Analytical Inc.) or a customized gas chromatograph (Shimadzu) equipped with a pulsed discharge helium ionization detector.

Material characterizations

Electron micrographs were acquired using a JEOL 1230 high-contrast transmission electron microscope operated at 80 kV and a JEOL 2100 field emission gun transmission electron microscope operated at 200 kV. HAADF-STEM images, electron tomography, and energy-dispersive x-ray were collected using a FEI Titan Themis3 (scanning) transmission electron microscope operated at 300 kV. HAADF-STEM tilt series images for electron tomography were acquired for Al@MIL-53 with tilt increments of 3° between an angular range of −66° to +72°. Before tomographic reconstruction, the tilt series images were aligned using the TomoJ plugin for FIJI (*42*). Tomographic reconstruction, also implemented with TomoJ in FIJI, was carried out using an iterative reconstruction algorithm of ordered subsets algebra reconstruction technique. Visualization and segmentation of the tomography reconstructions were carried out using Avizo V9.3 (Visualization Sciences Group). The 3D renderings in the main text, supporting movie S1, were generated in orthographic view. SEM images were acquired using a FEI Helios 660 NanoLab scanning electron microscope operated at an accelerating voltage of 5 to 10 kV and a working distance of 5 mm. Ultraviolet-visible (UV-Vis) extinction spectra were recorded by a Cary 5000 UV-Vis-NIR spectrometer in reflection mode. Dark-field measurements were carried out in a reflection mode using a custom-built instrument in the Halas laboratory, capable of measuring from 200 to 700 nm. Samples were measured with a 5-nm step size and 5-s integration time. Scattering measurements were correlated to scanning electron microscope images taken on a FEI Quanta 650 scanning electron microscope. Gas sorption studies were performed using a Quantachrome Autosorb-iQ automated gas sorption analyzer. N_2 sorption was performed at 77 K up to 1 bar, and CO_2 sorption was done at 273 K up to 1 bar. The samples were activated by heating under vacuum at 423 K for 4 hours before the sorption measurements. PXRD patterns of the activated nanoparticle powders were recorded with a Rigaku D/Max Ultima II diffractometer configured with a vertical θ/θ goniometer using Cu Kα radiation (λ = 1.5406 Å). To assess the thermal stability of the MIL-53(Al) MOF formed around Al NCs, a dry powder of Al@MOF (~10 mg) was heated under argon flow (100 cm^3 min^{-1}) from room temperature to 800°C with a ramp rate of 10°C min^{-1}. The weight of the sample was monitored by TGA analysis using a Q600 thermogravimetric analyzer. Raman spectra were acquired in ambient atmosphere under an excitation wavelength of 785 nm using a Renishaw inVia Raman microscope. Spectra of each sample were averaged over 50 scans and were baseline-subtracted on the basis of a built-in function of the instrument. A commercial FTIR spectrometer (Bruker Vertex 80v/Hyperion 3000 microscope) equipped with a mercury-cadmium-telluride detector was used to perform infrared spectroscopy.

SUPPLEMENTARY MATERIALS

Fig. S1. Crystal structure of the MIL-53(Al) MOF formed around Al NC.
Fig. S2. Vibrational spectroscopy of the MIL-53(Al) framework surrounding Al NC core.
Fig. S3. TGA analysis of Al NC@MIL-53(Al).
Fig. S4. Transmission electron microscopy characterizations of pristine Al NCs and Al NC@MIL-53(Al).
Fig. S5. Scanning electron microscopy characterizations of pristine Al NCs and Al NC@MIL-53(Al).
Fig. S6. Attempt for the synthesis of MIL-53(Al) shell around Al NCs following previously established synthetic strategy.
Fig. S7. Influence of the initial pH of the solution on formation of MIL-53(Al) around Al NCs.
Fig. S8. Time-dependent UV-Vis extinction spectrum of the reaction mixture during MIL-53(Al) shell formation around Al NCs.
Fig. S9. The role of organic linker on establishing MOF shell during hydrothermal dissolution of Al NC.
Fig. S10. Influence of sodium acetate on MOF formation progress.
Fig. S11. Pore size distribution of MIL-53(Al) shell layer around Al NC core.
Fig. S12. Spectrum of the light source used for photocatalysis and optical characterization of Al NC@MIL-53(Al) on γ-Al_2O_3 support.
Fig. S13. Product selectivity for thermally driven rWGS.
Fig. S14. Applying the dissolution-and-growth approach to Al NCs in a solution of 1,4-NDC.
Fig. S15. Applying the dissolution-and-growth approach to Al NCs in a solution of H_3BTC.
Fig. S16. Enhanced stability of Al NC in water through rational MOF coating.
Fig. S17. Coupling catalytically active TM nanoparticle islands to the Al@MOF hybrid for future photocatalytic applications.
Movie S1. 3D reconstruction of Al NC@MIL-53(Al) particle morphology using electron tomography.
References (*43–45*)

REFERENCES AND NOTES

1. H. Masatake, When gold is not noble: Catalysis by nanoparticles. *Chem. Rec.* **3**, 75–87 (2003).
2. A. Kwangjin, G. A. Somorjai, Size and shape control of metal nanoparticles for reaction selectivity in catalysis. *ChemCatChem* **4**, 1512–1524 (2012).
3. K. Watanabe, D. Menzel, N. Nilius, H.-J. Freund, Photochemistry on metal nanoparticles. *Chem. Rev.* **106**, 4301–4320 (2006).
4. M. J. Kale, T. Avanesian, P. Christopher, Direct photocatalysis by plasmonic nanostructures. *ACS Catal.* **4**, 116–128 (2014).
5. Y. Zhang, S. He, W. Guo, Y. Hu, J. Huang, J. R. Mulcahy, W. D. Wei, Surface-plasmon-driven hot electron photochemistry. *Chem. Rev.* **118**, 2927–2954 (2018).
6. H. Furukawa, K. E. Cordova, M. O'Keeffe, O. M. Yaghi, The chemistry and applications of metal-organic frameworks. *Science* **341**, 1230444 (2013).
7. P. Falcaro, R. Ricco, C. M. Doherty, K. Liang, A. J. Hill, M. J. Styles, MOF positioning technology and device fabrication. *Chem. Soc. Rev.* **43**, 5513–5560 (2014).
8. G. Lu, S. Li, Z. Guo, O. K. Farha, B. G. Hauser, X. Qi, Y. Wang, X. Wang, S. Han, X. Liu, J. S. DuChene, H. Zhang, Q. Zhang, X. Chen, J. Ma, S. C. J. Loo, W. D. Wei, Y. Yang, J. T. Hupp, F. Huo, Imparting functionality to a metal–organic framework material by controlled nanoparticle encapsulation. *Nat. Chem.* **4**, 310–316 (2012).
9. K. M. Choi, D. Kim, B. Rungtaweevoranit, C. A. Trickett, J. T. D. Barmanbek, A. S. Alshammari, P. Yang, O. M. Yaghi, Plasmon-enhanced photocatalytic CO2 conversion within metal–organic frameworks under visible light. *J. Am. Chem. Soc.* **139**, 356–362 (2017).
10. M. J. Meziani, C. E. Bunker, F. Lu, H. Li, W. Wang, E. A. Guliants, R. A. Quinn, Y.-P. Sun, Formation and properties of stabilized aluminum nanoparticles. *ACS Appl. Mater. Interfaces* **1**, 703–709 (2009).
11. M. Jérôme, P. Jérôme, Fabrication of aluminium nanostructures for plasmonics. *J. Phys. D Appl. Phys.* **48**, 184002 (2015).
12. B. D. Clark, C. R. Jacobson, M. Lou, J. Yang, L. Zhou, S. Gottheim, C. J. DeSantis, P. Nordlander, N. J. Halas, Aluminum nanorods. *Nano Lett.* **18**, 1234–1240 (2018).
13. M. B. Gawande, A. Goswami, F.-X. Felpin, T. Asefa, X. Huang, R. Silva, X. Zou, R. Zboril, R. S. Varma, Cu and Cu-based nanoparticles: Synthesis and applications in catalysis. *Chem. Rev.* **116**, 3722–3811 (2016).
14. U. Guler, S. Suslov, A. V. Kildishev, A. Boltasseva, V. M. Shalaev, Colloidal plasmonic titanium nitride nanoparticles: Properties and applications. *Nanophotonics* **4**, 269–276 (2015).
15. C. Rossi, Two decades of research on nano-energetic materials. *Propellants Explos. Pyrotech.* **39**, 323–327 (2014).
16. F. Cheng, P.-H. Su, J. Choi, S. Gwo, X. Li, C.-K. Shih, Epitaxial growth of atomically smooth aluminum on silicon and its intrinsic optical properties. *ACS Nano* **10**, 9852–9860 (2016).
17. B. Cerjan, X. Yang, P. Nordlander, N. J. Halas, Asymmetric aluminum antennas for self-calibrating surface-enhanced infrared absorption spectroscopy. *ACS Photonics* **3**, 354–360 (2016).
18. S. Tian, O. Neumann, M. J. McClain, X. Yang, L. Zhou, C. Zhang, P. Nordlander, N. J. Halas, Aluminum nanocrystals: A sustainable substrate for quantitative SERS-based DNA detection. *Nano Lett.* **17**, 5071–5077 (2017).
19. T. Gong, J. N. Munday, Aluminum-based hot carrier plasmonics. *Appl. Phys. Lett.* **110**, 021117 (2017).
20. J. Olson, A. Manjavacas, L. Liu, W.-S. Chang, B. Foerster, N. S. King, M. W. Knight, P. Nordlander, N. J. Halas, S. Link, Vivid, full-color aluminum plasmonic pixels. *Proc. Natl. Acad. Sci. U.S.A.* **111**, 14348–14353 (2014).
21. D. Franklin, Y. Chen, A. Vazquez-Guardado, S. Modak, J. Boroumand, D. Xu, S.-T. Wu, D. Chanda, Polarization-independent actively tunable colour generation on imprinted plasmonic surfaces. *Nat. Commun.* **6**, 7337 (2015).

22. L. Zhou, Y. Tan, J. Wang, W. Xu, Y. Yuan, W. Cai, S. Zhu, J. Zhu, 3D self-assembly of aluminium nanoparticles for plasmon-enhanced solar desalination. *Nat. Photonics* **10**, 393–398 (2016).

23. L. Zhou, C. Zhang, M. J. McClain, A. Manjavacas, C. M. Krauter, S. Tian, F. Berg, H. O. Everitt, E. A. Carter, P. Nordlander, N. J. Halas, Aluminum nanocrystals as a plasmonic photocatalyst for hydrogen dissociation. *Nano Lett.* **16**, 1478–1484 (2016).

24. D. F. Swearer, H. Zhao, L. Zhou, C. Zhang, H. Robatjazi, J. M. P. Martirez, C. M. Krauter, S. Yazdi, M. J. McClain, E. Ringe, E. A. Carter, P. Nordlander, N. J. Halas, Heterometallic antenna–reactor complexes for photocatalysis. *Proc. Natl. Acad. Sci. U.S.A.* **113**, 8916–8920 (2016).

25. H. Robatjazi, H. Zhao, D. F. Swearer, N. J. Hogan, L. Zhou, A. Alabastri, M. J. McClain, P. Nordlander, N. J. Halas, Plasmon-induced selective carbon dioxide conversion on earth-abundant aluminum-cuprous oxide antenna-reactor nanoparticles. *Nat. Commun.* **8**, 27 (2017).

26. F. Xia, J. Brugger, G. Chen, Y. Ngothai, B. O'Neill, A. Putnis, A. Pring, Mechanism and kinetics of pseudomorphic mineral replacement reactions: A case study of the replacement of pentlandite by violarite. *Geochim. Cosmochim. Acta* **73**, 1945–1969 (2009).

27. J. Reboul, S. Furukawa, N. Horike, M. Tsotsalas, K. Hirai, H. Uehara, M. Kondo, N. Louvain, O. Sakata, S. Kitagawa, Mesoscopic architectures of porous coordination polymers fabricated by pseudomorphic replication. *Nat. Mater.* **11**, 717–723 (2012).

28. M. J. McClain, A. E. Schlather, E. Ringe, N. S. King, L. Liu, A. Manjavacas, M. W. Knight, I. Kumar, K. H. Whitmire, H. O. Everitt, P. Nordlander, N. J. Halas, Aluminum nanocrystals. *Nano Lett.* **15**, 2751–2755 (2015).

29. T. Loiseau, C. Serre, C. Huguenard, G. Fink, F. Taulelle, M. Henry, T. Bataille, G. Férey, A rationale for the large breathing of the porous aluminum terephthalate (MIL-53) upon hydration. *Chem. Eur. J.* **10**, 1373–1382 (2004).

30. A. Sobhani, A. Manjavacas, Y. Cao, M. J. McClain, F. J. García de Abajo, P. Nordlander, N. J. Halas, Pronounced linewidth narrowing of an aluminum nanoparticle plasmon resonance by interaction with an aluminum metallic film. *Nano Lett.* **15**, 6946–6951 (2015).

31. G. Furrer, W. Stumm, The coordination chemistry of weathering: I. Dissolution kinetics of δ-Al_2O_3 and BeO. *Geochim. Cosmochim. Acta* **50**, 1847–1860 (1986).

32. Y. Zhao, N. Kornienko, Z. Liu, C. Zhu, S. Asahina, T.-R. Kuo, W. Bao, C. Xie, A. Hexemer, O. Terasaki, P. Yang, O. M. Yaghi, Mesoscopic constructs of ordered and oriented metal–organic frameworks on plasmonic silver nanocrystals. *J. Am. Chem. Soc.* **137**, 2199–2202 (2015).

33. M. D. Franke, W. R. Ernst, A. S. Myerson, Kinetics of dissolution of alumina in acidic solution. *AICHE J.* **33**, 267–273 (1987).

34. N. Cabrera, N. F. Mott, Theory of the oxidation of metals. *Rep. Prog. Phys.* **12**, 163–184 (1949).

35. S. Linic, U. Aslam, C. Boerigter, M. Morabito, Photochemical transformations on plasmonic metal nanoparticles. *Nat. Mater.* **14**, 567–576 (2015).

36. P. Christopher, H. Xin, A. Marimuthu, S. Linic, Singular characteristics and unique chemical bond activation mechanisms of photocatalytic reactions on plasmonic nanostructures. *Nat. Mater.* **11**, 1044–1050 (2012).

37. K. S. W. Sing, D. H. Everett, R. A. W. Haul, L. Moscou, R. A. Pierotti, J. Rouquérol, Reporting physisorption data for gas/solid systems with special reference to the determination of surface area and porosity (Recommendations 1984). *Pure Appl. Chem.* **57**, 603–619 (1985).

38. K. Sumida, D. L. Rogow, J. A. Mason, T. M. McDonald, E. D. Bloch, Z. R. Herm, T.-H. Bae, J. R. Long, Carbon dioxide capture in metal–organic frameworks. *Chem. Rev.* **112**, 724–781 (2012).

39. M. Mihaylov, K. Chakarova, S. Andonova, N. Drenchev, E. Ivanova, A. Sabetghadam, B. Seoane, J. Gascon, F. Kapteijn, K. Hadjiivanov, Adsorption forms of CO_2 on MIL-53(Al) and NH2-MIL-53(Al) as revealed by FTIR spectroscopy. *J. Phys. Chem. C* **120**, 23584–23595 (2016).

40. D. F. Swearer, R. K. Leary, R. Newell, S. Yazdi, H. Robatjazi, Y. Zhang, D. Renard, P. Nordlander, P. A. Midgley, N. J. Halas, E. Ringe, Transition-metal decorated aluminum nanocrystals. *ACS Nano* **11**, 10281–10288 (2017).

41. E. Palik, *Handbook of Optical Constants of Solids* (Academic Press, 1985).

42. C. Messaoudil, T. Boudier, C. O. S. Sorzano, S. Marco, TomoJ: Tomography software for three-dimensional reconstruction in transmission electron microscopy. *BMC Bioinformatics* **8**, 288 (2007).

43. A. E. J. Hoffman, L. Vanduyfhuys, I. Nevjestić, J. Wieme, S. M. J. Rogge, H. Depauw, P. Van Der Voort, H. Vrielinck, V. Van Speybroeck, Elucidating the vibrational fingerprint of the flexible metal–organic framework MIL-53(Al) using a combined experimental/computational approach. *J. Phys. Chem. C* **122**, 2734–2746 (2018).

44. A. Comotti, S. Bracco, P. Sozzani, S. Horike, R. Matsuda, J. Chen, M. Takata, Y. Kubota, S. Kitagawa, Nanochannels of two distinct cross-sections in a porous al-based coordination polymer. *J. Am. Chem. Soc.* **130**, 13664–13672 (2008).

45. T. Loiseau, L. Lecroq, C. Volkringer, J. Marrot, G. Férey, M. Haouas, F. Taulelle, S. Bourrelly, P. L. Llewellyn, M. Latroche, MIL-96, a porous aluminum trimesate 3D structure constructed from a hexagonal network of 18-membered rings and ^{μ3}-oxo-centered trinuclear units. *J. Am. Chem. Soc.* **128**, 10223–10230 (2006).

Citation: H. Robatjazi, D. Weinberg, D. F. Swearer, C. Jacobson, M. Zhang, S. Tian, L. Zhou, P. Nordlander, N. J. Halas, Metal-organic frameworks tailor the properties of aluminum nanocrystals. *Sci. Adv.* **5**, eaav5340 (2019).